Published in final edited form as:
NMR Biomed. 2016 September ; 29(9): 1249–1257. doi:10.1002/nbm.3581.

CEST of the Cervical Spinal Cord at 7 Tesla

Adrienne N. Dula[a,c,†], **Siddharama Pawate**[b], **Lindsey M. Dethrage**[c], **Benjamin N. Conrad**[c], **Blake E. Dewey**[d], **Robert L. Barry**[a,c], and **Seth A. Smith**[a,c,e,f]

[a]Department of Radiology and Radiological Sciences, Vanderbilt University Medical Center, Nashville, TN, USA

[b]Department of Neurology, Vanderbilt University Medical Center, Nashville, TN, USA

[c]Vanderbilt University Institute of Imaging Science, Vanderbilt University Medical Center, Nashville, TN, USA

[d]National Institutes of Health, NINDS, Vanderbilt University Medical Center, Nashville, TN, USA

[e]Department of Biomedical Engineering, Vanderbilt University Medical Center, Nashville, TN, USA

[f]Department of Neuroscience, Vanderbilt University Medical Center, Nashville, TN, USA

Abstract

High-magnetic field (7T) chemical exchange saturation transfer (CEST) MRI provides information regarding tissue biochemical environment. Multiple sclerosis (MS) affects the entire central nervous system including the spinal cord. Optimal CEST saturation parameters found via simulation were implemented for CEST MRI in ten healthy controls and ten MS patients and results were examined using traditional asymmetry analysis and Lorentzian fit method. Additionally, T_1- and T_2*-weighted images were acquired for lesion localization and the transmitted B_1^+ field was evaluated to guide imaging parameters.

Distinct spectral features for all tissue types studied were found both up- and down-field from the water resonance. The z-spectra in healthy subjects had the expected z-spectra shape with CEST effects apparent from 2.0 ppm – 4.5 ppm. The z-spectra from MS patients demonstrated deviations from this expected, normal shape indicating this method's sensitivity to known pathology as well as those tissues appearing normal on conventional MRI. Examination of the calculated $CEST_{asym}$ reveals increased asymmetry around the amide proton resonance ($\Delta\omega$ = 3.5 ppm) but it is apparent that this measure is complicated by detail in the CEST spectrum up-field from water, which is expected to result from Nuclear Overhauser effect. The z-spectra up field (negative ppm range) are also distinct between healthy and diseased tissue and cannot be ignored, particularly when considering the conventional asymmetry analysis used to quantify the CEST effect. For all frequencies greater than +1 ppm, the Lorentzian difference (and z-spectra) for lesions and normal appearing white matter are distinct from healthy white matter.

[†]Corresponding Author: Adrienne N. Dula, Vanderbilt University Institute of Imaging Science, 1161 21st Ave South, Nashville, TN 37232, Adrienne.n.dula@vanderbilt.edu, Phone: 615-343-0471, Fax: 615-322-0734.

The increased frequency separation and signal to noise (SNR) in concert with prolonged T_1 at 7T result in signal enhancements necessary to detect subtle tissue changes not possible at lower field strengths. This study presents CEST imaging metrics that may be sensitive to the extensive and temporally varying biochemical neuropathology of MS in the spinal cord.

Keywords

spinal cord; chemical exchange saturation transfer; multiple sclerosis

Introduction

Magnetic Resonance Imaging (MRI) has been crucial to understanding the radiological presentation of multiple sclerosis (MS), aiding in diagnosis, tracking disease evolution, and evaluation of treatment efficacy. The spinal cord is the relay center for the nervous system, a vital link between brain and body. The spinal cord is somatotopically organized, creating an opportunity to study the direct correlation between structure and function, which is an ideal realm to better understand the mechanisms that lead to clinical dysfunction. MS is an autoimmune/degenerative disease of the central nervous system affecting over 2.5 million people worldwide and is characterized by focal regions of demyelination and inflammation, readily apparent on MRI. One challenge, however is that MS is clinically, radiologically, and functionally variable among individuals and over time, all of which are not consistently reflected in imaging measures. There is a critical need for alternative, robust biomarkers of disease manifestation and progression. A second challenge is that often, the radiological focus is on the brain and conventional MRI findings do not always correlate well with clinical symptoms of sensory or motor dysfunction. Lastly, we recognize that MS significantly involves the spinal cord (1,2), and to that end, much of the disability in MS is thought to be derived from spinal cord lesions (3–5). We hypothesize that there is a need to develop high-resolution, disease-sensitive, quantitative MRI methods for the spinal cord in patients with MS.

However, the spinal cord is difficult to evaluate using advanced MRI techniques due to technical limitations. The spinal cord's small diameter (~15mm), smaller internal structures, and constant motion demand high-resolution motion-insensitive methods. Often conventional MRI of the spinal cord results in motion artifacts due to cardiac and respiratory movement as well as susceptibility artifacts due to spatially periodic field inhomogenietites from surrounding bone and cartilage. Additionally, partial volume effects frequently preclude quantitative MRI measurements of segmented tissue, particularly at low field. To characterize neurological deficits such as those caused by MS, MRI studies in both the clinic and research settings have utilized semi-quantitative indices such as T_1- or T_2-weighted lesion burden (6,7), presence (or absence) of contrast-enhancing lesions (8,9), and tissue atrophy (10) with equivocal results. Extension to more advanced measures such as magnetization transfer (MT) imaging and diffusion weighted imaging (11,12) have resulted in strengthened correlations with sensorimotor function due to their sensitivity to tissue microstructure. Unfortunately, these techniques applied at lower fields such as 3T still suffer from long acquisition times, low signal to noise ratio (SNR) and poor resolutions significantly impacted by partial volume effects.

We present the development of high-magnetic field (7T) chemical exchange saturation transfer (CEST) MRI technique to study the spinal cord in patients with MS. CEST spectrum, or z-spectrum (13), is acquired by applying off-resonance radio frequency (RF) saturation to labile protons and detecting attenuation of the water signal as a function of offset frequency. The rationale is that CEST methods can be used to explore the labile protons found on tissue metabolites (14,15), thereby providing an indirect measurement of these biochemicals which are known to be altered in MS (16). Although MR spectroscopy of the spinal cord can report on tissue metabolites (17), this technique at any field strength faces significant challenges of shimming, small volumes of interest, and poor spectral fidelity. Thus there is a need for improved methods to assess changes to the spinal cord that may predate overt lesion formation, gross inflammation and tissue loss. CEST, however, has rarely been studied in the spinal cord, and has not been explored in the spinal cord of patients with MS. Recently, CEST MRI has been applied to the spinal cord at 3T for the purpose of examining the asymmetry of magnetization transfer (18), and Kogan et al. implemented glutamate CEST (GluCEST) to examine the exchange related properties of glutamate at the high-cervical levels of C1–C2 at 7T (19). We present application of CEST MRI to the cervical spinal cord *in vivo* in healthy controls and MS patients clinically noted to have deficits localized to the spinal cord. We focus our attention on optimization of the saturation prepulse and evaluation of the B_1^+ transmit field for evaluation of primarily the amide proton transfer (APT) resonances, but also resonances reflective of amine and hydroxyl moieties, while minimizing scan time for patient populations. These targets were chosen because the represent known biological relevance to multiple sclerosis (i.e. amide proton transfer: protein accumulation in normal appearing white mater and alternations in neurochemicals such as glutamate and myoinositol). Optimal pulse parameters for amide proton transfer found via simulation were implemented in healthy controls and MS patients and results were examined using traditional asymmetry analysis and the Lorentzian fit method proposed by Jones et al. (20). To our knowledge, this is the first description of the CEST spectra in the spinal cord of patients with MS.

Experimental

Simulations

Simulations were based on the thesis work by Blake Dewey (21) and designed to identify optimal CEST preparation (RF irradiation power and bandwidth) parameters for contrast from chemical exchange occurring 3.5 ppm downfield from water (amide proton transfer, APT) in healthy spinal cord tissue at 7T. All simulations were carried out utilizing the scripting environment in MATLAB 2014b (Mathworks, Natick, Massachusetts) on an Apple iMac (Cupertino, CA; 3.0 GHz, dual core CPU). Theoretical saturation was modeled according to the Bloch equations for three pools: bulk water (free), semisolid macromolecular (conventional MT), and mobile macromolecular (CEST) pools. This was achieved using the simple matrix solution to numerically solve the Bloch equations (22),

$$\frac{d\mathrm{M}}{dt}=\mathrm{A}\cdot\mathrm{M}, where \qquad \mathrm{M}=[M_x(t)\ M_y(t)\ M_z(t)\ 1]^T\ and$$

$$A=\begin{bmatrix} -R_2 & \Delta\omega & 0 & 0 \\ -\Delta\omega & -R_2 & \omega_1 & 0 \\ 0 & -\omega_1 & -R_1 & R_1M_0 \\ 0 & 0 & 0 & 0 \end{bmatrix}. \qquad [1]$$

Using the matrix exponential, $\mathbf{M}(t)=e^{At}\mathbf{M}(0)$, this can be solved by determining the eigenvalues and eigenvectors for A. This base can be expanded to consider the three pools (23) incorporating the effect of exchange (CEST) and confounding effects of magnetization transfer (22) using:

$$A=\begin{bmatrix} -(R_2^a+k_{ab}) & k_{ba} & \Delta\omega_a & 0 & 0 & 0 & 0 & 0 \\ k_{ab} & -(R_2^a+k_{ba}) & 0 & \Delta\omega_b & 0 & 0 & 0 & 0 \\ -\Delta\omega_a & 0 & -(R_2^a+k_{ab}) & k_{ba} & \omega_1 & 0 & 0 & 0 \\ 0 & -\Delta\omega_b & k_{ab} & -(R_2^a+k_{ba}) & 0 & \omega_1 & 0 & 0 \\ 0 & 0 & -\omega_1 & 0 & -(R_2^a+k_{ab}+k_{ac}) & k_{ba} & k_{ca} & R_1^aM_0^a \\ 0 & 0 & 0 & -\omega_1 & k_{ab} & -(R_1^b+k_{ba}) & 0 & R_1^bM_0^b \\ 0 & 0 & 0 & 0 & k_{ac} & 0 & -(R_1^c+k_{ca}+W(\Delta\omega)) & R_1^cM_0^c \\ 0 & 0 & 0 & 0 & 0 & 0 & 0 & 0 \end{bmatrix}$$

[2]

The superscripts *a*, *b*, and *c* denote the three pools: water, solute, and macromolecular or MT components. This simulation assumes a T_2-dependent Super-Lorentzian absorption lineshape for the macromolecules and is contained in the parameter W(Δω) (24). Physical values (T_1, T_2, k_{ex}, concentration, chemical shift) were fixed according to (25,26). The bulk water was modeled as a Lorentzian with T_1/T_2 = 1538 ms/45 ms based on previous relaxation measures at 3T in the spinal cord white matter (27) and modified for 7T expectations. The semisolid macromolecular pool was modeled with $T_1/T_2/k_{ex}$ = 1000 ms/10 **μ**s/50 Hz with $\Delta\omega = -2.34$ ppm (28). The mobile solute pool, or CEST pool, was modeled as a Lorentzian with $T_1/T_2/k_{ex}$ = 1600 ms/20 ms/20 Hz with $\Delta\omega = +3.5$ ppm with a concentration of 0.001 (M_o^b) compared to the bulk water ($M_o^a = 1.000$) and MT (M_o^c = 0.100).

We simulated the impact of various RF saturation parameters (offset, power, and duration) on the signal magnitude of the APT effect, which was assessed at $\Delta\omega = 3.5$ ppm downfield from water. For the pulse sequence, we chose to use the pulsed CEST approach (29), which utilizes a single RF irradiation for every repetition time (TR) to build up a steady state CEST effect over multiple short TR's. Therefore our simulations included a single RF irradiation, a brief delay for spoiling, an on-resonance excitation, and a delay for readout. The B_1

amplitude (power) was varied over amplitudes from 0 μT to 3 μT while holding the duration constant at 25 ms. The B_1 amplitude was subsequently fixed to 1 μT while the pulse duration was varied from 0 ms to 55 ms.

Participants

All studies were approved by the local Institutional Review Board, were HIPPA compliant, and included informed consent obtained using REDCap software (30). Participants included ten healthy volunteers (2 female) ranging between 20–47 years old (mean ± std = 33 ± 10 years) and ten patients clinically diagnosed with relapsing-remitting multiple sclerosis (RRMS) (6 female) ranging between 21–49 years (mean ± std = 40 ± 7 years). The MS patients were recruited from a tertiary clinic by their attending neurologist. The Expanded Disability Status Scale (EDSS) (31) was measured within two weeks of the MRI exam. Specific patient demographics are found in Table 1.

Magnetic Resonance Imaging

All data were obtained using a whole body 7T Philips Achieva scanner (Philips Medical Systems, Cleveland, OH) using a surface quadrature coil and 16-channel spine array (Nova Medical, Wilmington, MA) for RF transmission and reception, respectively, at the level of cervical vertebrae C2–C4. Data acquisitions included anatomical T_1-weighted imaging and T_2^*-weighted imaging in the axial plane, B_1^+ and ΔB_0 field mapping, and CEST MRI. T_1-weighted images were acquired using a 3D fast field echo with a SENSE factor of 2 in the AP direction. TR/TE/flip/bandwidth = 30 ms/3.6 ms/60°/505.8 Hz resulting in a scan time of 5:03 minutes. T_2^*-weighted images were acquired with multislice, fast gradient echo readout with TR/TE/flip/bandwidth = 305 ms/9.1 ms/25°/115.9 Hz with an acquisition time of 5:02 minutes. These axial images were acquired at $0.6 \times 0.6 \times 4.0$ mm^3 and reconstructed to $0.29 \times 0.29 \times 4.0$ mm^3.

Evaluation of B_1^+ Field

The B_1^+ field of the spinal cord coil is expected to vary axially with distance from the surface coils and also rostral-caudal along the length of the cord. When designing saturation, it is important to gauge the magnitude of this variation and thus we evaluated the homogeneity in transmit field, B_1^+ using a 3D fast field echo readout with a dual T_R (extension of 125 ms) method over the same field of view as the CEST data and the B_1^+ calculated according to Yarnykh et al. (32). Maps were calculated from images acquired using a 3D fast field echo with TR/TE/flip /bandwidth = 35 ms/2.7 ms/60°/506.1 Hz at $2.68 \times 2.68 \times 4.0$ mm^3 resolution and reconstructed to $0.67 \times 0.67 \times 4.0$ mm^3. The right-left and anterior-posterior B_1^+ was measured in the center slice (C3) and rostral-caudal, longitudinal B_1^+ was measured along a 40 mm volume covering C2–C4 vertebral levels. Percentage of the prescribed flip angle was calculated and compared both among all subjects as well as between healthy subjects and MS patients using the Mann-Whitney U test.

CEST MRI

CEST data were acquired on all participants using the pulsed CEST approach (29), which utilizes a single RF pulse, every TR to establish a steady state CEST effect over multiple short *TR's*. The CEST sequence was performed in the axial plane using a multi-shot 3D gradient echo with multi-shot EPI (factor of 7), TR/TE/flip = 65 ms/7.2 ms/5°. The image resolution was 1.5 × 1.6 × 5.0 mm^3 (AP x RL x FH) using sensitivity encoding in RL and FH directions (factor = 2) over a field of view of 150 × 150 × 165 mm^3 (AP ×RL × FH). Fat suppression was accomplished using a binomial excitation pulse resulting in a scan time of 5.46 s per image. Saturation parameters were chosen based on the results of simulation and preliminary B_1^+ field evaluations. This resulted in a 25-ms duration Gaussian-windowed pulse with peak B_1 = 2 μT resulting in an approximate duty cycle of 40%. Spoiler gradients were applied, using maximum gradient strength, after every CEST RF irradiation, prior to excitation as discussed in the simulation section. Saturation off-resonance frequencies ($\Delta\omega$) were varied from $\Delta\omega = -40$ to 40 ppm sampled in random order (same for each subject) to avoid residual saturation effects with increased sampling around offsets of interest including 0 ppm and ±3.5 ppm with an S_0 image ($\Delta\omega = +80$ ppm) acquired every five offsets for characterization and correction of baseline drift (33) resulting in a total of 64 distinct image data sets. The saturation offsets (in ppm) included: ±40.00, ±20.00, ±10.00, ±9.00, ±8.00, ±7.00, ±6.00, ±5.00, ±4.75, ±4.50, ±4.25, ±4.00, ±3.75, ±3.50, ±3.25, ±3.00, ±2.75, ±2.50, ±2.25, ±2.00, ±1.50, ±1.00, ±0.75, ±0.50, ±0.25, 0.00, 0.01, as well as 12 acquisitions at 80.00 interspersed throughout the sequence. To ensure steady state, readout was set to begin at the high frequency end of k-space as 49 TR's are required to achieve steady state.

CEST Data Processing

All data were processed in Matlab R2014b (The Mathworks, Natick, MA). CEST data were co-registered (34) to the first CEST volume ($\Delta\omega = +80$ ppm) using the FMRIB's Linear Image Registration Tool (FLIRT), a 12 degree of freedom 3D affine algorithm to optimize the correlation ratio in FSL (35,36). To minimize registration of unwanted signals outside the spinal cord, we applied a Gaussian weighting kernel of 100 voxels (standard deviation of 50), centered on the spinal cord region. Following registration, each CEST-weighted voxel was normalized to the time-varying signal intensity derived resulting from saturation far off resonance, $S_0 = S(\Delta\omega = 80 \text{ ppm})$ similar to that used by Jones *et al.* (37) to account for signal drift as follows: non-CEST-weighted signal intensities (S_0), acquired every 32 seconds, were analyzed by fitting a cubic spline to the voxel-wise signal variation as a function of scan time and the calculated S_0 values were used for signal normalization where *z*-spectrum = $S(\Delta\omega)/S_0$. The *z*-spectra were then fit to a Lorentzian function including only the data from saturation frequency offsets $\Delta\omega > 10$ ppm and $\Delta\omega < 1$ ppm. The minima of this fit were assigned the water frequency ($\Delta\omega = 0$ ppm). Z-spectra were shifted accordingly to account for inhomogeneities in the B_0 field.

The CEST effect was quantified using two different methods. The classic spectral asymmetry was calculated by directly comparing the opposing sides of the centered *z*-spectra with respect to the water frequency (38) using:

$$CEST_{asym}(\Delta\omega)=[S(-\Delta\omega)-S(\Delta\omega)]/S_0 \quad [3]$$

Additionally, the CEST effect was examined using the difference between the Lorentzian fit (20,39) and the normalized data at $\Delta\omega = 3.5$ ppm.

Regions of interest (ROIs) were manually outlined in axial slices to include the entire spinal cord from cervical levels C2–C4. For tissue-specific analyses, ROIs were also drawn within these slices to include white matter, gray matter, and lesions. Mean spectra were calculated from each subject for evaluation of the population variance. These spectra were then averaged across populations for comparison between healthy subjects and those affected by MS. Further analysis included calculation of overall mean and 95% confidence intervals (CI) for the CEST effect at 3.5 ppm in healthy subjects.

Results

Simulations

Optimal CEST preparation parameters (RF irradiation power and bandwidth) for contrast from amide proton exchange occurring 3.5 ppm downfield from water in healthy spinal cord tissue at 7T were determined based on the results of simulations. The simulated CEST effect at 3.5 ppm downfield from water is shown as a function of pulse duration and amplitude in Figure 1, with the maximum CEST effect due to amide protons found for pulse amplitudes of 0.5 μT to 3.0 μT within the pulse duration range of 15 – 30 ms. As expected, there is a tradeoff between short and strong pulses (best for achieving sufficient saturation) and longer and weaker pulses with a narrower bandwidth to more specifically elicit the APT CEST effect. Optimal parameters were chosen to minimize scan time (pulse duration) while observing all safety guidelines due to power deposition and specific absorption rate limitations. Therefore, a saturation duration of 25 ms was chosen to maintain a short scan time with an expected APT effect greater than 4%. Simulations also predicted that a pulse amplitude of 1 μT at 25 ms was optimal.

Evaluation of B_1^+ Field

The measured B_1^+ field was considerably less than that prescribed throughout the field of view. Figure 2 depicts the average variation of B_1^+ in all volunteers across the spinal cord in the right-left (A), anterior-posterior (B), and foot-head (C) directions. The percent of the prescribed flip angle ranged from 15.5% to 82.0% with a mean (± standard deviation) of 50.6% (± 13.1%). To achieve the desired pulse amplitude of 1 μT, a 2 μT pulse was prescribed assuming an average B_1^+ of approximately 50%. The mean percentage of prescribed flip angle for the relevant ROIs in healthy subjects was 49.65% ± 14.5% and that for the MS patients was 53.25% ± 12.2%. These values were not significantly different at $\alpha = 0.05$ with $p = 4.6 \times 10^{-26}$.

CEST MRI: Healthy Subjects

Example data from a healthy subject are shown in Figure 3; Panel A shows the T_2*-weighted sagittal slice through the cervical spinal cord, Panel B and C display T_1- and T_2^*-weighted axial slices through the center of the field of view at the level between C2–C3. Panel D shows CEST results from a region of interest encompassing the entire spinal cord at the level of C2/3 with this ROI shaded yellow in Panels B and C. The normalized CEST spectrum (S/S_0) is shown as a function of the saturation offset frequency (blue, solid) with the Lorentzian fit to this data shown as a dashed blue line. There are a few interesting features of this spectrum including downfield deviations from the Lorentizan fit around 4 ppm and 2.5 ppm, as shown by the red dashed line. To quantify the CEST effect, the calculated $CEST_{asym}$ (red, solid) and Lorentzian difference (red, dashed) are also plotted as a function of saturation frequency offset. Examination of the calculated $CEST_{asym}$ reveals an increased asymmetry around the amide proton resonance ($\Delta\omega$ = 3.5 ppm) but it is apparent that this measure is complicated by detail in the CEST spectrum up field from the water resonance, which is expected to result from Nuclear Overhauser effect (NOE).

CEST MRI: Multiple Sclerosis Patients

Group mean spectra from MS patients are compared to that of healthy subjects in Figure 4. The mean z-spectra (± standard deviation) of the healthy subjects (blue, solid line) and that of MS patients (red, solid line) are shown as well as the respective mean Lorentzian difference spectra (dashed lines). These spectra were derived from whole cord ROIs between C2–C4. The mean Lorentzian difference in healthy subjects demonstrates CEST effects around $\Delta\omega$ = +2–3 ppm and +3.5–4.5 ppm while that for MS patients are less apparent. From figure 4, we can also see that there are spectral resonances (such as at $\Delta\omega$ = 4.2 ppm and 2.0ppm) where there are more pronounced differences between patients and healthy volunteers, which is encouraging for future studies. We expect that the resonance at 4.2 might be shifted due to reduced exchange rate in the spinal cord, but we focus the rest of our analysis on resonances which are hypothesized to reflect more specific biological processes.

In order to begin to establish a clinically significant change in CEST effects Figure 5 depicts the mean and 95% confidence intervals (CIs) of the measured whole cord Lorentzian difference at the amide resonance ($\Delta\omega$ = 3.5 ppm) for the ten healthy subjects. Figure 4 shows the variation of the healthy controls. Individual patient results are shown in comparison to appreciate pathological results against the consistency of the healthy subject data in Figure 5. It is important to note that we do not necessarily expect consistent results from the patient data as MS is variable from patient to patient.

In order to further examine the frequency distributions of CEST measures in the spinal cord of MS patients, pixel-wise histogram analyses were performed, Figure 6. ROI's were selected in lesion, NAWM, and GM for one slice in each MS patient (n = 10). The Lorentzian difference was measured at three frequency offsets including that of the amide protons (3.5 ppm) in Panel A, as well as those resonances associated with the amine protons (3.0 ppm) in Panel B and 2.0 ppm in Panel C. The x-axis depicts the calculated CEST effect (Lorentzian difference) while the y-axis is the frequency of pixels demonstrating that CEST effect. This frequency was calculated as the number of overall pixels which fell into those bins normalized to the total number of pixels found in each region of interest across MS patients. The ROI sizes were (in number of voxels): Lesion = 174, NAWM = 201, and GM = 177. It is apparent that the different tissue types exhibit interesting and distinct features at each resonance indicating the wealth of information obtained in the entire z-spectra. For instance, at 3.5 ppm (Panel A), the gray matter (blue) appears uni-modally distributed with a median similar to that of normal appearing white matter (green). Both the lesion (red) and

NAWM (green) appear left-skewed due to bi-modal distributions. At 3.0 ppm, normal appearing white matter and gray matter exhibit a similar CEST effect, roughly normal and centered at approximately 0.05, while the lesion is significantly lower in signal intensity and broader. At 2.0 ppm, little to no difference is observed in the peak amplitude and spread among tissue types as the characteristics of the CEST effects seem to converge for these tissue types at 2.0 ppm (Panel C). Overall, it is valuable to examine various saturation-offset frequencies in order to appreciate the complex characteristics of MS pathology in the cervical spinal cord.

Discussion

CEST MRI is a valuable, non-invasive tool which has been utilized as a biomarker for various pathologies in the brain, and other organ systems. However, as a biomarker of MS pathologies, CEST has been unexplored in the spinal cord at 7T, and only two current publications have documented CEST in the spinal cord (18,19). Here, we present an optimized, rapid, CEST acquisition for the spinal cord at 7T and report features of the CEST spectra in healthy subjects and MS patients. The spinal cord exhibits limited redundancy, plasticity, or compensation for damage, creating an exemplary platform for quantitative MRI innovation. Although MS neuropathy affects the entire central nervous system, focus is typically on brain despite evidence that 80% of MS patients have spinal cord involvement (2,42).

However, the nature of the spinal cord precludes quantitative MRI. It measures only approximately 1.5 cm across while its location creates problematic motion and susceptibility differences due to pulsation of surrounding cerebrospinal fluid and presence of large vertebrae. Migration to 7T permits the higher resolution scans that are imperative to evaluation of specific regions of interest within the cervical spinal cord. The presented study achieved in-plane resolution of 1.5 mm × 1.6 mm for CEST data acquisition in 5 minutes. Consequently, increased field strength does not come without complications as RF inhomogeneity, susceptibility, and power deposition all increase with increased B_0. These issues have been addressed using preliminary assessment of transmitted field; optimization based on simulations and advanced image acquisition methods.

Preliminary evaluation of the transmitted RF field indicated the actual flip angle in side the spinal cord (deep to the coil elements) was only a fraction of that prescribed. To offer a first order mitigation for this, we increased amplitude of the saturation pulse to ensure that the appropriate power (for APT effects) was achieved inside the spinal cord tissue studied by simulations (Figure 1). Thus, according to the evaluation of the transmitted B_1^+ field (Figure 2) we adjusted the amplitude of the saturation pulse to 2 μT in order to obtain a 1 μT amplitude deep in the cord, since the mean flip angle was only 50.6% of that prescribed. Although this evaluation of the B_1^+ field did reveal aberrations from the prescribed power, we did not see significant in-plane or through-plane variation in the cord itself that would warrant B_1^+ inhomogeneity correction such as that presented by Singh, et al. (43). Additionally, we recognize that B_1^+ field variations such as those seen here can confound measurements between healthy and patient cohorts. A brief analysis of the correlation between B_1^+ and measured APT effect showed that the measured APT effect in patients and volunteers did not differ based on B1 alone. Lastly, we should point out that one challenge with this particular coil arrangement and the principle reason that the B1 in the cord itself is low is the power deposition to the surface of the skin. Since the B_1^+ decreases deep in the tissue, increasing the drive scale or maximum amplitude of the transmit chain would cause local hot-spots at the surface of the neck and posing a danger to the participant. For those reasons, we chose, to a first order approximation, to drive the amplitude of the saturation pulse higher, recognizing that the decrease in B_1^+ in the spinal cord will affect all RF in our transmit chain.

Motion correction is essential for data acquired on the time scale of CEST MRI. The presented CEST MRI method achieved a 5.46 second dynamic scan time resulting in an acquisition time of 5 minutes. The CEST-weighted images were Gaussian-windowed and co-registered using an affine registration algorithm optimized for the spinal cord. This algorithm performed adequately even in the presence of dynamic contrast changes such as those found within CEST MRI data. Additionally, the acquisition parameters were carefully chosen in order to minimize motion-induced artifacts while also limiting deposited power. A segmented echo planar readout with a short TR allowed for rapid data acquisition while building up to the steady state (20). This data acquisition method adheres to the scanner hardware limitations while minimizing saturation pulse duration to permit a feasible imaging time. Additionally, the pulse duration of 25 ms results in a 40% duty cycle, the optimal setting for observing CEST contrast (44). Fluctuations in S_0 were de-trended as previously described (37), in order to maintain an accurate baseline for the z-spectral analysis.

It should also be pointed out that when examining the spinal cord at 7T, especially with CEST acquisitions, three areas need to be carefully considered: 1) the FOV of the 3D volume, 2) the nature of spoiling, and 3) the method and volume of B0 shimming. Importantly for small 3D volumes, with poor spoiling and higher-order B0 shimming, back-folding of the acquisition and the RF saturation can occur which is convolved on the z-spectrum of interest. Thus, it is important to assure that spoiling be performed, as in our case, using the highest available gradient amplitude after ever RF saturation pulse. Additionally, while the 3D volume of imaging was large enough to minimize any 3D wrap,[20] we chose to shim over a smaller FOV. In our protocol, we utilized higher-order shimming (3rd order) over a prescribed FOV that covered from C1 to C7 over the anterior and posterior aspects of the vertebral canal while minimizing visual contact with the airways, lungs, or anterior structures of the neck. This provided a shim that performed well over the spinal cord, but we do recognize the impact that this shimming routine will have for CEST saturation outside the well-shimmed regions.

Overall CEST results indicate differences between healthy and pathological spinal cord tissue over much of the spectral range in the corrected z-spectra. Figure 4 indicates a trend toward distinct spectral features between healthy and MS spinal cord, particularly down-field from the water resonance. The z-spectra in healthy subjects had the expected shape with CEST effects apparent from 2.0 ppm – 4.5 ppm while CEST effects were more prominent in MS patients between 1.0 ppm – 2.0 ppm. Of particular interest are the CEST effects at the amide resonance (3.5 ppm) and further analysis at this resonance is displayed in Figure 5. It is apparent that most patient data fall below the CIs of the healthy subjects. In order to examine this variation, the APT effect size was compared to B_1^+ measures confirming the lack of influence of B_1^+ on the variation present in APT measures ($R = 0.3502$, $P = 0.2311$).

In order to estimate the natural variance of the CEST measurements in healthy subjects, the overall mean (solid, black line) and 95% confidence intervals (dashed, black line) for the ten healthy subjects were calculated and plotted in Figure 5. To examine how MS patients compared to this accepted range of healthy tissue, the measured CEST effect at 3.5 ppm is plotted for each MS patient. This demonstrates that 70% of the MS patients examined do not fall within the confidence intervals calculated for healthy subjects, with the majority of these measures having a lower CEST effect at the amide resonance. This demonstrates the unique characteristics of each MS patient as patient results are not expected to be consistent as the disease varies from patient to patient as well as over time.

The z-spectra from MS patients demonstrated intra-patient deviations as well as differences from that of healthy subjects, indicating this method’s sensitivity to known pathology as well as those tissues appearing normal on conventional MRI. While all MS tissue types demonstrate CEST effects beginning around 1.5 ppm down-field from water, the normal appearing white matter demonstrates a wider range of deviations down-field including saturation frequency offsets up to 4.5 ppm. This broadening of the CEST effect around the expected metabolites (including amide and amine protons) could be a result of the short saturation pulse used but could also be reflective of known underlying tissue pathology.

We have a few limitations to our study. Although we do not anticipate our acquisition sequence to be sensitive to the effects of fat (due to binomial fat suppression), MT or the NOE we do observe exchange-mediated NOE in all of the examined tissue types. These NOE are convolved with the CEST effects when the asymmetry measures are performed, but it is evident that these will have varying contributions as seen in Panel D of Figure 3 as well as Figure 4, ultimately making interpretation of the CEST asymmetry very difficult. Group differences were observed in Figure 6A, with obviously different spectral features found between the healthy tissue (blue) and MS patients (red). Albeit the many features of the CEST spectrum creating differences between MS patients and healthy controls, an additional limitation of this study is that the proposed method focused on only a couple of those features. The parameters of the saturation pulse were optimized to examine the APT effect at 3.5 ppm downfield from water. It is interesting to note that with these particular parameters, more information is contained in the spinal cord CEST z-spectra than was previously expected from brain examinations such as the CEST effects seen at 4.2 ppm. We are enthusiastic about the potential for further study, which will focus on a complete spectral analysis of CEST effects in a patient population.

Extended evaluation of the Lorentzian difference at 3.5 ppm, 3.0 ppm, and 2.0 ppm for the MS patients indicates the rich amount of data contained in the range down-field from the water resonance. The increased frequency separation and SNR in concert with prolonged T_1 at 7T result in signal enhancements necessary to detect subtle tissue changes not possible at lower field strengths. This study presents CEST imaging metrics that may be sensitive to the extensive and temporally varying biochemical neuropathology of MS in the spinal cord.

Acknowledgments

The authors would like to acknowledge all of the patients and subjects who volunteered for our study. We would also like to acknowledge funding sources: NIH/NIBIB K01EB009120, NIH/NIBIB K25 EB013659, KL2 TR 000446 and CTSA Grant (RR024975).

Abbreviations

MS	multiple sclerosis
MT	magnetization transfer
CEST	chemical exchange saturation transfer
gluCEST	glutamate CEST
APT	amide proton transfer
RF	radio frequency
NOE	nuclear Overhauser effect
EDSS	expanded disability status scale

References

1. Bergers E, Bot JC, van der Valk P, Castelijns JA, Lycklama a Nijeholt GJ, Kamphorst W, Polman CH, Blezer EL, Nicolay K, Ravid R, Barkhof F. Diffuse signal abnormalities in the spinal cord in multiple sclerosis: direct postmortem in situ magnetic resonance imaging correlated with in vitro high-resolution magnetic resonance imaging and histopathology. Annals of neurology. 2002; 51(5): 652–656. [PubMed: 12112117]
2. Kidd D, Thorpe JW, Thompson AJ, Kendall BE, Moseley IF, MacManus DG, McDonald WI, Miller DH. Spinal cord MRI using multi-array coils and fast spin echo. II. Findings in multiple sclerosis. Neurology. 1993; 43(12):2632–2637. [PubMed: 8255468]
3. Lycklama a Nijeholt GJ, Castelijns JA, Lazeron RH, van Waesberghe JH, Polman CH, Uitdehaag BM, Barkhof F. Magnetization transfer ratio of the spinal cord in multiple sclerosis: relationship to atrophy and neurologic disability. Journal of neuroimaging : official journal of the American Society of Neuroimaging. 2000; 10(2):67–72. [PubMed: 10800258]
4. Filippi M. Non-conventional MR techniques to monitor the evolution of multiple sclerosis. Neurological sciences : official journal of the Italian Neurological Society and of the Italian Society of Clinical Neurophysiology. 2001; 22(2):195–200.
5. Oh J, Zackowski K, Chen M, Newsome S, Saidha S, Smith SA, Diener-West M, Prince J, Jones CK, Van Zijl PC, Calabresi PA, Reich DS. Multiparametric MRI correlates of sensorimotor function in the spinal cord in multiple sclerosis. Mult Scler. 2013; 19(4):427–435. [PubMed: 22891033]
6. Schreiber K, Sorensen PS, Koch-Henriksen N, Wagner A, Blinkenberg M, Svarer C, Petersen HC. Correlations of brain MRI parameters to disability in multiple sclerosis. Acta Neurol Scand. 2001; 104(1):24–30. [PubMed: 11442439]
7. Brex PA, Ciccarelli O, O'Riordan JI, Sailer M, Thompson AJ, Miller DH. A longitudinal study of abnormalities on MRI and disability from multiple sclerosis. N Engl J Med. 2002; 346(3):158–164. [PubMed: 11796849]
8. Bot JC, Barkhof F, Polman CH, Lycklama a Nijeholt GJ, de Groot V, Bergers E, Ader HJ, Castelijns JA. Spinal cord abnormalities in recently diagnosed MS patients: added value of spinal MRI examination. Neurology. 2004; 62(2):226–233. [PubMed: 14745058]
9. Klawiter EC, Benzinger T, Roy A, Naismith RT, Parks BJ, Cross AH. Spinal cord ring enhancement in multiple sclerosis. Arch Neurol. 2010; 67(11):1395–1398. [PubMed: 21060017]

10. Kearney H, Rocca M, Valsasina P, Balk L, Sastre-Garriga J, Reinhardt J, Ruggieri S, Rovira A, Stippich C, Kappos L, Sprenger T, Tortorella P, Rovaris M, Gasperini C, Montalban X, Geurts J, Polman C, Barkhof F, Filippi M, Altmann D, Ciccarelli O, Miller D, Chard D. Magnetic resonance imaging correlates of physical disability in relapse onset multiple sclerosis of long disease duration. Mult Scler. 2013
11. Oh J, Zackowski K, Chen M, Newsome S, Saidha S, Smith SA, Diener-West M, Prince J, Jones CK, Van Zijl PC, Calabresi PA, Reich DS. Multiparametric MRI correlates of sensorimotor function in the spinal cord in multiple sclerosis. Mult Scler. 2013; 19(4):427–435. [PubMed: 22891033]
12. Zackowski KM, Smith SA, Reich DS, Gordon-Lipkin E, Chodkowski BA, Sambandan DR, Shteyman M, Bastian AJ, van Zijl PC, Calabresi PA. Sensorimotor dysfunction in multiple sclerosis and column-specific magnetization transfer-imaging abnormalities in the spinal cord. Brain. 2009; 132(Pt 5):1200–1209. [PubMed: 19297508]
13. Bryant RG. The dynamics of water-protein interactions. Annual review of biophysics and biomolecular structure. 1996; 25:29–53.
14. Ward KM, Aletras AH, Balaban RS. A new class of contrast agents for MRI based on proton chemical exchange dependent saturation transfer (CEST). Journal of Magnetic Resonance. 2000; 143(1):79–87. [PubMed: 10698648]
15. Zhou JY, Payen JF, Wilson DA, Traystman RJ, van Zijl PCM. Using the amide proton signals of intracellular proteins and peptides to detect pH effects in MRI. Nature Medicine. 2003; 9(8):1085–1090.
16. Soares DP, Law M. Magnetic resonance spectroscopy of the brain: review of metabolites and clinical applications. Clinical radiology. 2009; 64(1):12–21. [PubMed: 19070693]
17. Ackerman JJ, Grove TH, Wong GG, Gadian DG, Radda GK. Mapping of metabolites in whole animals by 31P NMR using surface coils. Nature. 1980; 283(5743):167–170. [PubMed: 7350541]
18. Ng MC, Hua J, Hu Y, Luk KD, Lam EY. Magnetization transfer (MT) asymmetry around the water resonance in human cervical spinal cord. Journal of magnetic resonance imaging : JMRI. 2009; 29(3):523–528. [PubMed: 19243033]
19. Kogan F, Singh A, Debrosse C, Haris M, Cai K, Nanga RP, Elliott M, Hariharan H, Reddy R. Imaging of glutamate in the spinal cord using GluCEST. NeuroImage. 2013; 77:262–267. [PubMed: 23583425]
20. Jones CK, Polders D, Hua J, Zhu H, Hoogduin HJ, Zhou J, Luijten P, van Zijl PC. In vivo three-dimensional whole-brain pulsed steady-state chemical exchange saturation transfer at 7 T. Magnetic resonance in medicine : official journal of the Society of Magnetic Resonance in Medicine / Society of Magnetic Resonance in Medicine. 2012; 67(6):1579–1589.
21. Dewey, BE. Simulation and Optimization of Pulsed Chemical Exchange Saturation Transfer for Clinical Application at 3T. Vanderbilt University; 2013. p. 73
22. Woessner DE, Zhang SR, Merritt ME, Sherry AD. Numerical solution of the Bloch equations provides insights into the optimum design of PARACEST agents for MRI. Magnetic Resonance in Medicine. 2005; 53(4):790–799. [PubMed: 15799055]
23. Desmond KL, Stanisz GJ. Understanding Quantitative Pulsed CEST in the Presence of MT. Magnetic Resonance in Medicine. 2012; 67(4):979–990. [PubMed: 21858864]
24. Morrison C, Stanisz G, Henkelman RM. Modeling magnetization transfer for biological-like systems using a semi-solid pool with a super-Lorentzian lineshape and dipolar reservoir. Journal of magnetic resonance Series B. 1995; 108(2):103–113. [PubMed: 7648009]
25. Rooney WD, Johnson G, Li X, Cohen ER, Kim SG, Ugurbil K, Springer CS Jr. Magnetic field and tissue dependencies of human brain longitudinal 1H2O relaxation in vivo. Magn Reson Med. 2007; 57(2):308–318. [PubMed: 17260370]
26. Michaeli S, Garwood M, Zhu XH, DelaBarre L, Andersen P, Adriany G, Merkle H, Ugurbil K, Chen W. Proton T2 relaxation study of water, N-acetylaspartate, and creatine in human brain using Hahn and Carr-Purcell spin echoes at 4T and 7T. Magn Reson Med. 2002; 47(4):629–633. [PubMed: 11948722]
27. Smith SA, Edden RA, Farrell JA, Barker PB, Van Zijl PC. Measurement of T1 and T2 in the cervical spinal cord at 3 tesla. Magnetic resonance in medicine : official journal of the Society of

Magnetic Resonance in Medicine / Society of Magnetic Resonance in Medicine. 2008; 60(1):213–219.

28. Hua J, Jones CK, Blakeley J, Smith SA, van Zijl PC, Zhou J. Quantitative description of the asymmetry in magnetization transfer effects around the water resonance in the human brain. Magnetic resonance in medicine : official journal of the Society of Magnetic Resonance in Medicine / Society of Magnetic Resonance in Medicine. 2007; 58(4):786–793.
29. Jones CK, Polders D, Hua J, Zhu H, Hoogduin HJ, Zhou J, Luijten P, van Zijl PC. In vivo three-dimensional whole-brain pulsed steady-state chemical exchange saturation transfer at 7 T. Magn Reson Med. 2012; 67(6):1579–1589. [PubMed: 22083645]
30. Harris PA, Taylor R, Thielke R, Payne J, Gonzalez N, Conde JG. Research electronic data capture (REDCap)–a metadata-driven methodology and workflow process for providing translational research informatics support. Journal of biomedical informatics. 2009; 42(2):377–381. [PubMed: 18929686]
31. Kurtzke JF. Rating neurologic impairment in multiple sclerosis: an expanded disability status scale (EDSS). Neurology. 1983; 33(11):1444–1452. [PubMed: 6685237]
32. Yarnykh VL. Actual flip-angle imaging in the pulsed steady state: a method for rapid three-dimensional mapping of the transmitted radiofrequency field. Magnetic resonance in medicine : official journal of the Society of Magnetic Resonance in Medicine / Society of Magnetic Resonance in Medicine. 2007; 57(1):192–200.
33. Yadav NN, Chan KW, Jones CK, McMahon MT, van Zijl PC. Time domain removal of irrelevant magnetization in chemical exchange saturation transfer Z-spectra. Magn Reson Med. 2013
34. Netsch T, van Muiswinkel A. Quantitative evaluation of image-based distortion correction in diffusion tensor imaging. IEEE Trans Med Imaging. 2004; 23(7):789–798. [PubMed: 15250631]
35. Jenkinson M, Smith S. A global optimisation method for robust affine registration of brain images. Medical image analysis. 2001; 5(2):143–156. [PubMed: 11516708]
36. Jenkinson M, Bannister P, Brady M, Smith S. Improved optimization for the robust and accurate linear registration and motion correction of brain images. NeuroImage. 2002; 17(2):825–841. [PubMed: 12377157]
37. Jones CK, Huang A, Xu J, Edden RA, Schar M, Hua J, Oskolkov N, Zaca D, Zhou J, McMahon MT, Pillai JJ, van Zijl PC. Nuclear Overhauser enhancement (NOE) imaging in the human brain at 7T. NeuroImage. 2013; 77:114–124. [PubMed: 23567889]
38. Guivel-Scharen V, Sinnwell T, Wolff SD, Balaban RS. Detection of proton chemical exchange between metabolites and water in biological tissues. J Magn Reson. 1998; 133(1):36–45. [PubMed: 9654466]
39. Dula AN, Arlinghaus LR, Dortch RD, Dewey BE, Whisenant JG, Ayers GD, Yankeelov TE, Smith SA. Amide proton transfer imaging of the breast at 3 T: establishing reproducibility and possible feasibility assessing chemotherapy response. Magnetic resonance in medicine : official journal of the Society of Magnetic Resonance in Medicine / Society of Magnetic Resonance in Medicine. 2013; 70(1):216–224.
40. Dousset V, Grossman RI, Ramer KN, Schnall MD, Young LH, Gonzalez-Scarano F, Lavi E, Cohen JA. Experimental allergic encephalomyelitis and multiple sclerosis: lesion characterization with magnetization transfer imaging. Radiology. 1992; 182(2):483–491. [PubMed: 1732968]
41. Hua J, Jones CK, Blakeley J, Smith SA, van Zijl PCM, Zhou JY. Quantitative description of the asymmetry in magnetization transfer effects around the water resonance in the human brain. Magnetic Resonance in Medicine. 2007; 58(4):786–793. [PubMed: 17899597]
42. Bergers E, Bot JC, van der Valk P, Castelijns JA, Lycklama a Nijeholt GJ, Kamphorst W, Polman CH, Blezer EL, Nicolay K, Ravid R, Barkhof F. Diffuse signal abnormalities in the spinal cord in multiple sclerosis: direct postmortem in situ magnetic resonance imaging correlated with in vitro high-resolution magnetic resonance imaging and histopathology. Annals of Neurology. 2002; 51(5):652–656. [PubMed: 12112117]
43. Singh A, Cai K, Haris M, Hariharan H, Reddy R. On B1 inhomogeneity correction of in vivo human brain glutamate chemical exchange saturation transfer contrast at 7T. Magnetic resonance in medicine : official journal of the Society of Magnetic Resonance in Medicine / Society of Magnetic Resonance in Medicine. 2013; 69(3):818–824.

44. Zu Z, Li K, Janve VA, Does MD, Gochberg DF. Optimizing pulsed-chemical exchange saturation transfer imaging sequences. Magnetic resonance in medicine : official journal of the Society of Magnetic Resonance in Medicine / Society of Magnetic Resonance in Medicine. 2011; 66(4): 1100–1108.

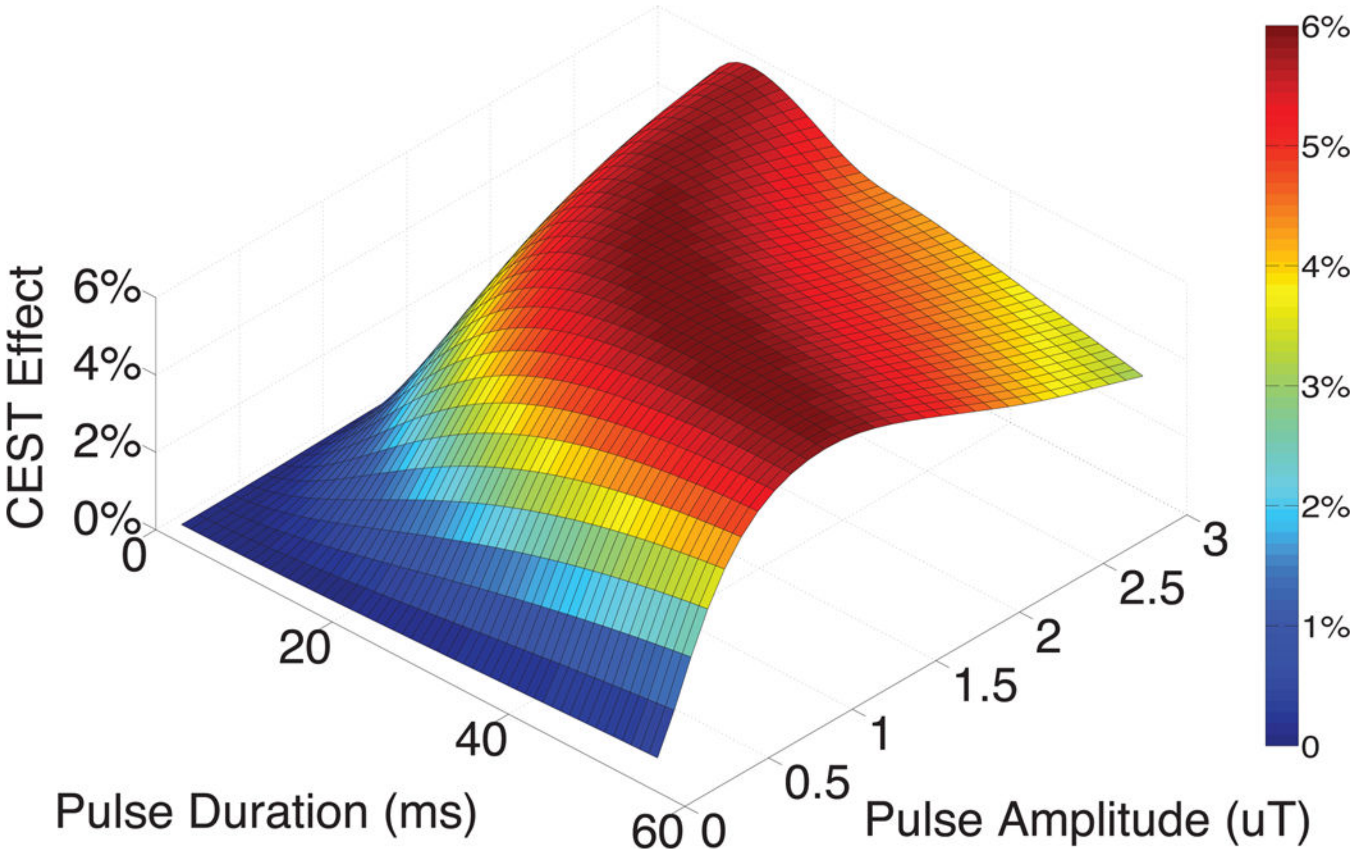

Figure 1.

Simulated CEST effect due to the presence of exchanging amide protons as a function of pulse duration and amplitude at 7 Tesla. The maximum amide proton transfer effect was found to occur with a pulse duration between 15 – 30 ms and pulse amplitudes of 0.5 μT – 3.0 μT. The saturation pulse parameters chosen for spinal cord CEST imaging were 25 ms duration and 2 μT amplitude (to account for B1+ effects).

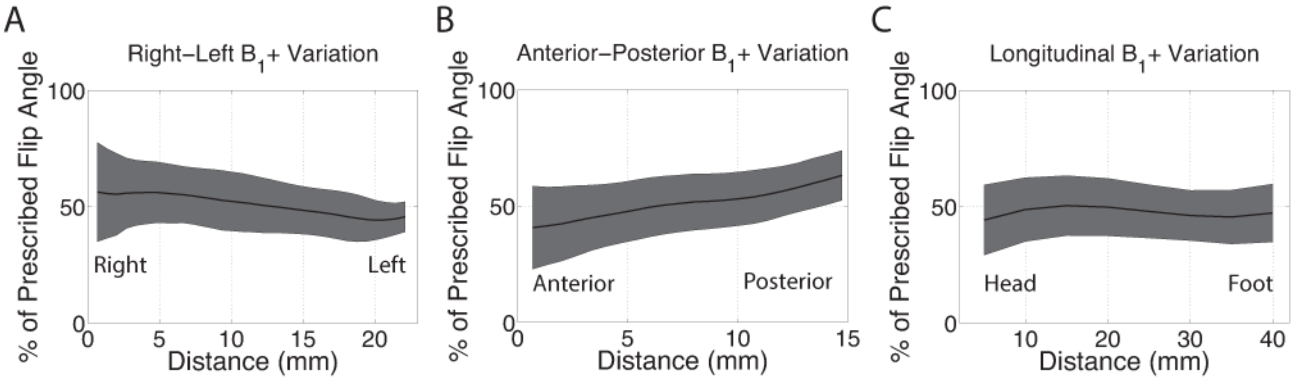

Figure 2.

The variation of B1+ through the axial (A), anterior-posterior (B), and longitudinal (C) directions as measured using dual-TR data. The percent of the prescribed flip angle ranged from 15.5% to 82.0% with a mean (± standard deviation) of 50.6% (± 13.1%).

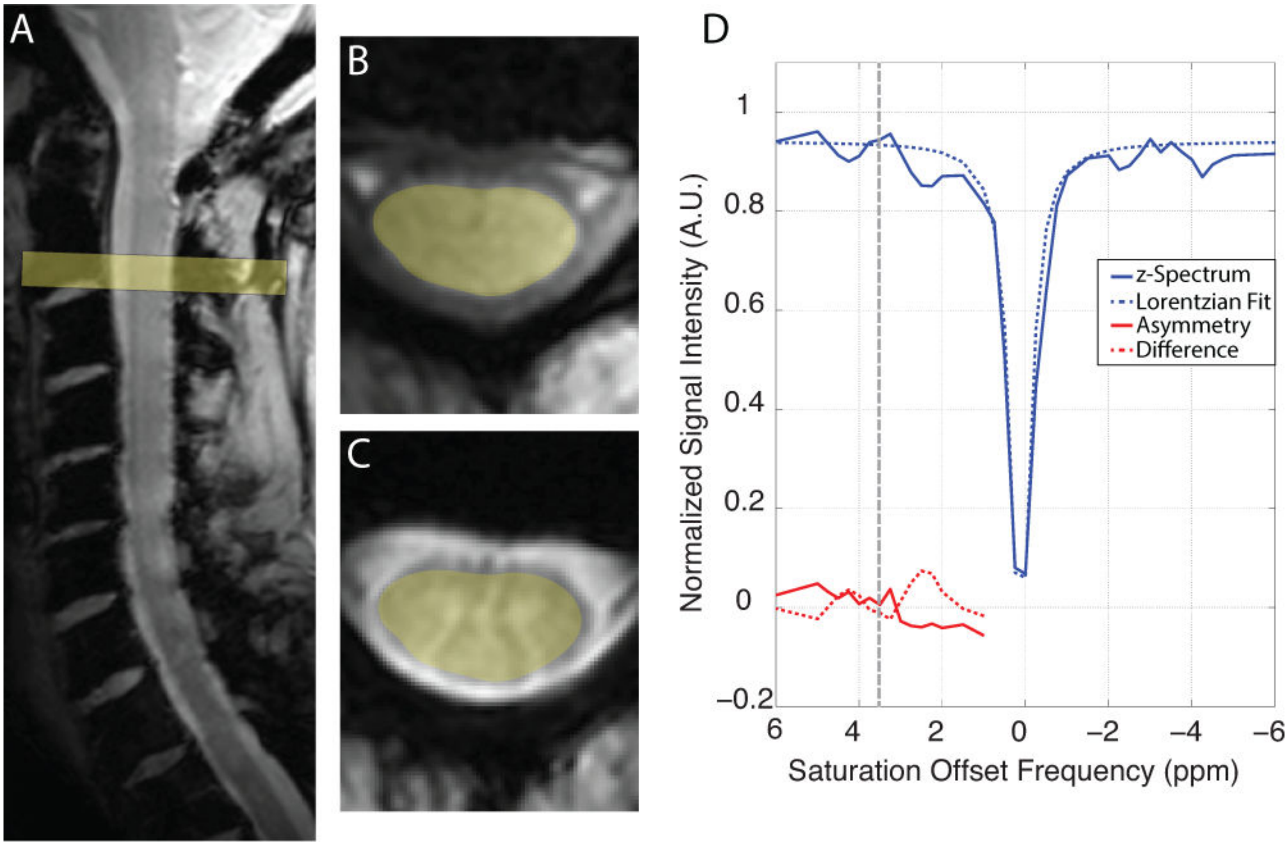

Figure 3.

Representative CEST data from a healthy subject scanned at 7 T. A) T2-weighted sagittal slice through the cervical spinal cord, B) T1-weighted axial slice and C) T2*-weighted axial slice through the center of the field of view at the level of C3. D) The z-spectrum (blue, solid) and Lorentzian fit (blue, dashed) from a region of interest encompassing the entire spinal cord are shown as a function of saturation offset frequency. Additionally, the calculated CESTasym (red, solid) and Lorentzian difference (red, dashed) are shown for comparison with 3.5 ppm denoted by the black dashed line.

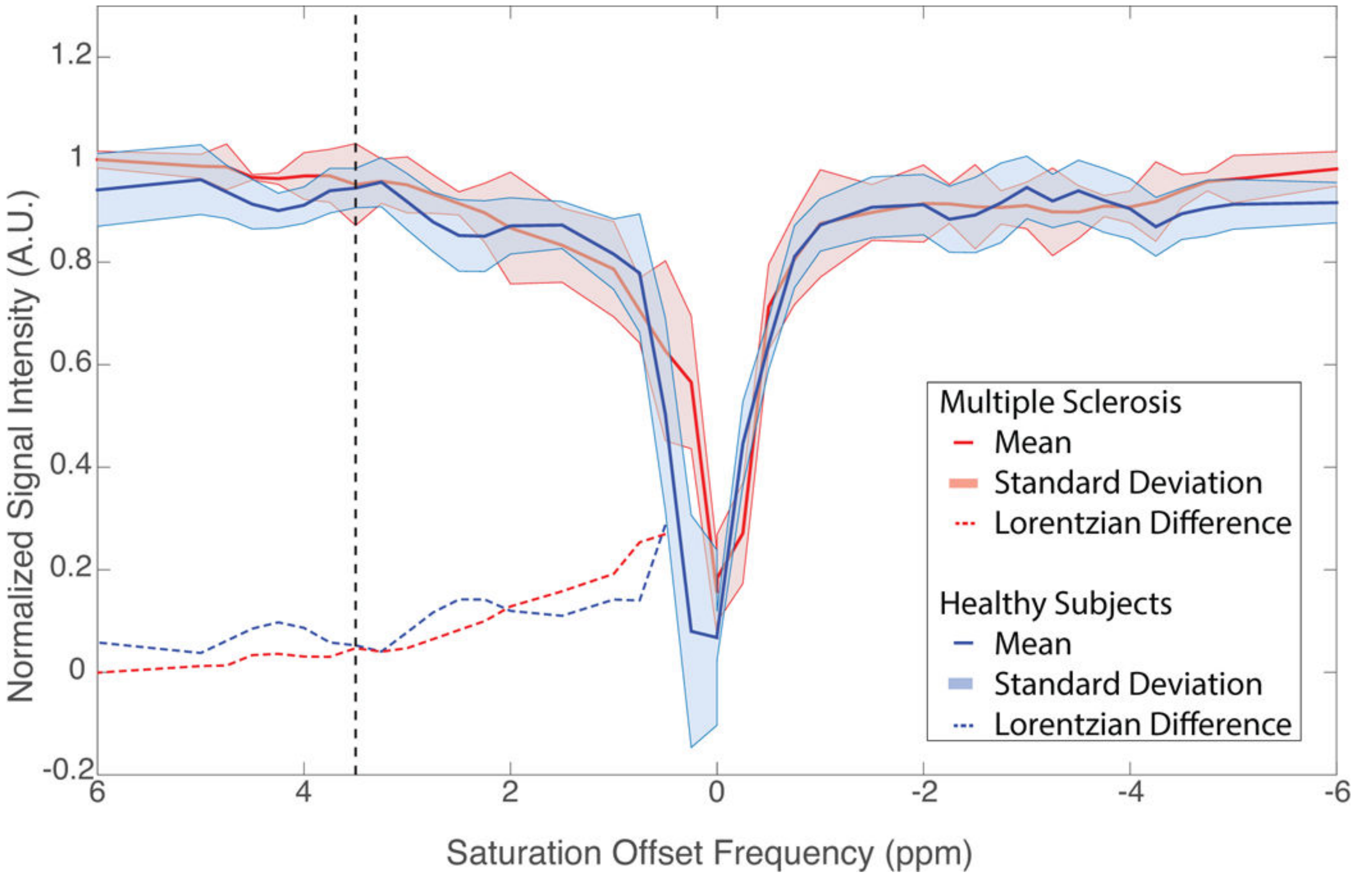

Figure 4.

Comprehensive results of CEST MRI in the spinal cord. Group mean (± standard deviation) z-spectra are shown for healthy subjects (blue, solid) and MS patients (red, solid). The calculated Lorentzian difference for these group mean z-spectra are plotted as dashed lines for the healthy subjects (blue) and MS patients (red). Healthy subjects show marked deviations from the Lorentzian fit at saturation offsets of +2 – +3 ppm and +3.5 – +4.5 ppm.

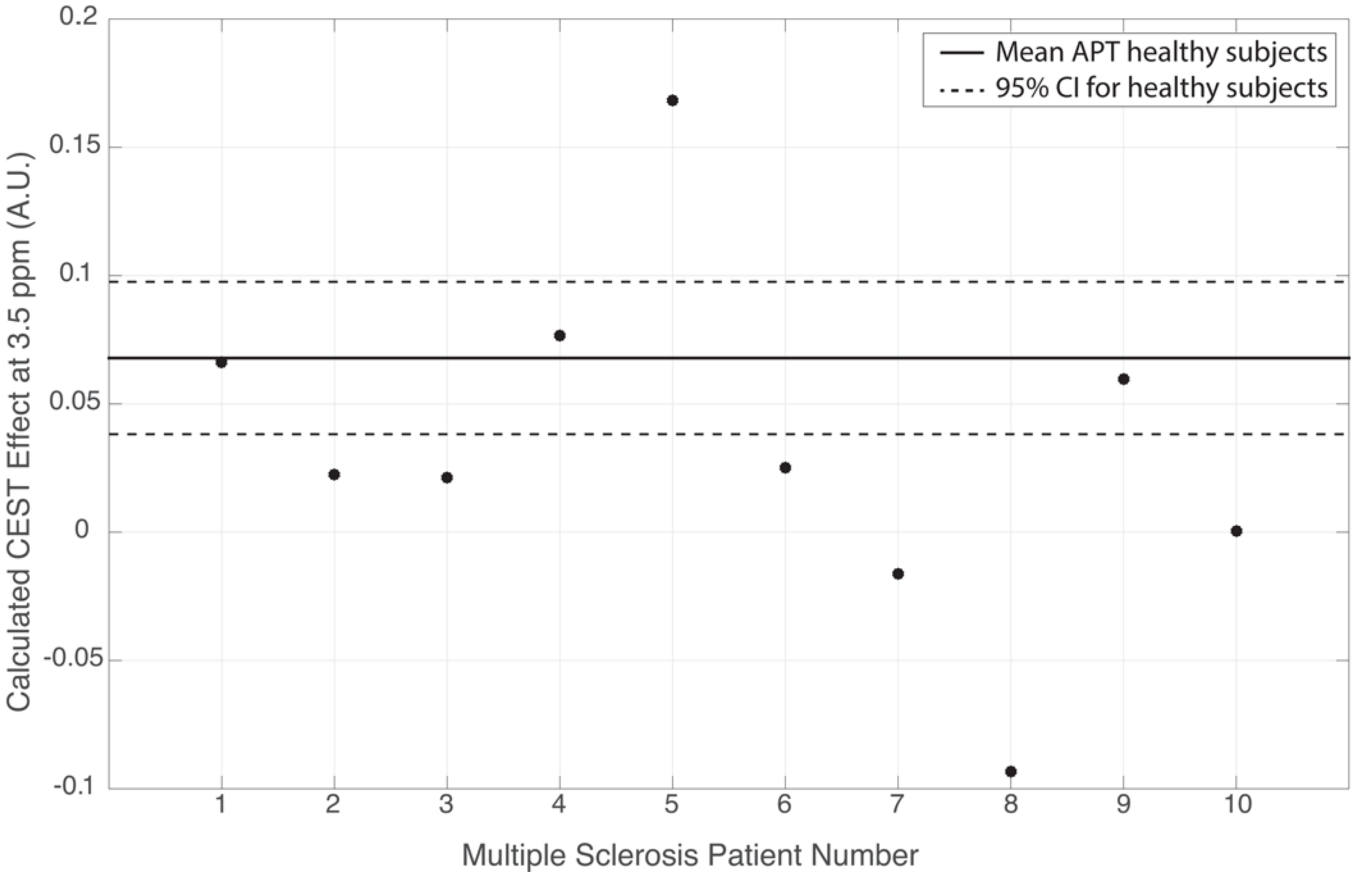

Figure 5.

Calculated CEST effect at 3.5 ppm (amide proton transfer, APT) for all MS patients shown in relation to calculated mean and 95% confidence intervals (CIs) for the ten healthy subjects.

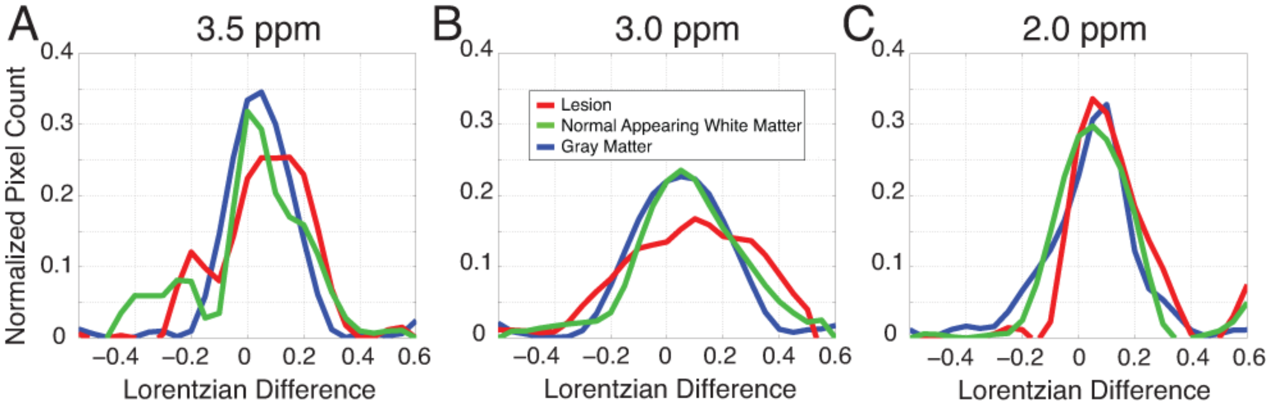

Figure 6.

Comprehensive data from all MS patients depicting pixel-wise analysis of the CEST effect at the saturation frequency offsets of 3.5 ppm (A), 3.0 ppm (B), and 2.0 ppm (C). Histograms are shown of the calculated Lorentzian difference normalized by the total number of pixels for regions of interest in lesion (red), normal appearing white matter (green), and gray matter (blue).

Table 1

Spinal Cord MRI Patients

Patient	EDSS	Age (years)	Duration (years)
MS 1	1	28	1
MS 2	1	43	23
MS 3	6	40	8
MS 4	2	48	7
MS 5	0	31	6
MS 6	1	44	9
MS 7	0	33	1
MS 8	3	49	8
MS 9	0	37	11
MS 10	0	21	5

EDSS: Expanded disability status scale score, MS: Multiple sclerosis,